Accepted Manuscript

Title: The Mechanism of Corrosion of Aluminium Zirconium Silicate (AZS) Material in the Float Glass Furnace Regenerator

Authors: S.M. George, P.W. Haycock, R.M. Ormerod

PII: S0955-2219(17)30814-2
DOI: https://doi.org/10.1016/j.jeurceramsoc.2017.12.006
Reference: JECS 11611

To appear in: *Journal of the European Ceramic Society*

Received date: 10-9-2017
Revised date: 30-11-2017
Accepted date: 4-12-2017

Please cite this article as: George SM, Haycock PW, Ormerod R.M.The Mechanism of Corrosion of Aluminium Zirconium Silicate (AZS) Material in the Float Glass Furnace Regenerator.*Journal of The European Ceramic Society* https://doi.org/10.1016/j.jeurceramsoc.2017.12.006

The Mechanism of Corrosion of Aluminium Zirconium Silicate (AZS) Material in the Float Glass Furnace Regenerator

Dr S. M. George[a], Professor P. W. Haycock[a], Professor R. M. Ormerod[a]

[a]Faculty of Natural Sciences, Keele University, Stoke-on-Trent, Staffordshire, ST5 5BG

Abstract
Failure mechanisms in AZS materials from the regenerators of two float glass furnaces are presented. Results of a post-mortem examination of materials are used to identify the physical and chemical changes during service. Methods used include bulk density and apparent porosity measurements, optical microscopy, scanning electron microscopy (SEM), elemental dispersive analysis (EDA), x-ray fluorescence spectroscopy (XRF), x-ray diffraction (XRD) and IR spectroscopy. Corrosion was found to be related to oxidising and reducing conditions and temperature. Chemical and physical differences between virgin and three different furnace materials are identified and used to propose a mechanism for corrosion in different zones of the glass furnace regenerator.

Keywords
AZS; Corrosion; Refractories; Regenerator; Failure

1. Introduction

Heat recovery is important for environmental and economic operation of the glass making furnace [1-6]. To reach melting temperatures of around 1600°C, a gas-fired regenerative furnace uses regenerators to transfer waste heat to incoming air. Waste gas is vented through the regenerator packing (checker bricks) transferring heat to the bricks whilst incoming air enters the melting tank via checkers on the other side. This preheats incoming air to around 800°C before it reaches the burners. The cycle is reversed every 20 minutes creating extreme, alternating thermal and oxidising conditions and steep temperature gradients within the regenerator (Figure 1). In addition, high velocity air flows carry corrosive gases from the melting tank and dust from the raw materials (batch). These substances cause severe wear and corrosion within the regenerator and blockage due to condensation [1].

Physical and chemical stability of regenerator materials is crucial. Fused cast, cruciform refractory materials made up of Al_2O_3, ZrO_2 and SiO_2 (AZS) are used in this application. The corrosion rate of an AZS refractory is proportional to its porosity and composition [7, 8]. A dense, low porosity microstructure ensures good thermal properties [9] while limiting chemical ingress of corrosive agents [10,11,12]. Strength [13,14] corrosion resistance and microstructural properties are affected by cooling rates during manufacture [15] and subsequent melting in service. Failure of these checkers can result in shut-down of the furnace with significant loss of production for the manufacture. This study discusses the mechanism of corrosion in AZS materials recovered from the middle (condensation) zone of the regenerators of two furnaces, F1and F2. Materials from three ports on both the left (L) and right (R) sides of the furnace were recovered from F1. Port 1 is near to the charging end and is subject to higher levels of batch dust carryover (Figure 2). Conditions in these ports can reach around 1620°C. The order of degradation was L3>L2>R3>R1>L1>R2 with R2 exhibiting the greatest resistance to service conditions.

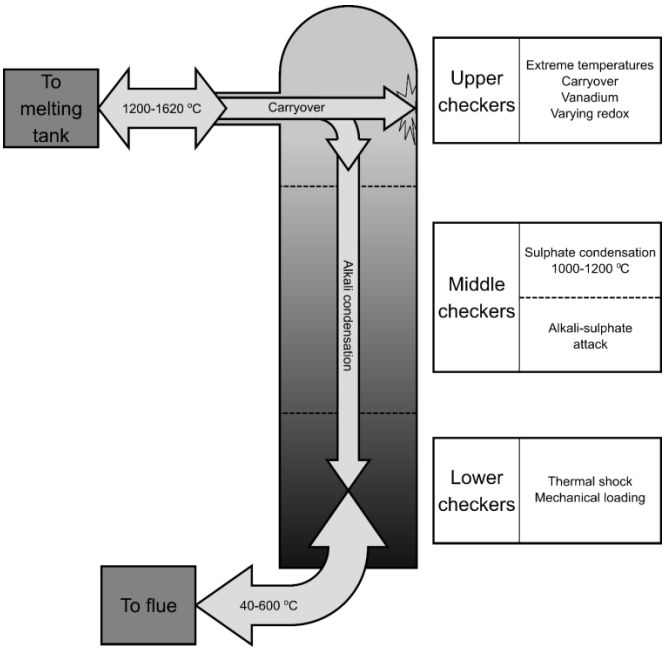

Figure 1. Diagram to show the zones within the regenerator

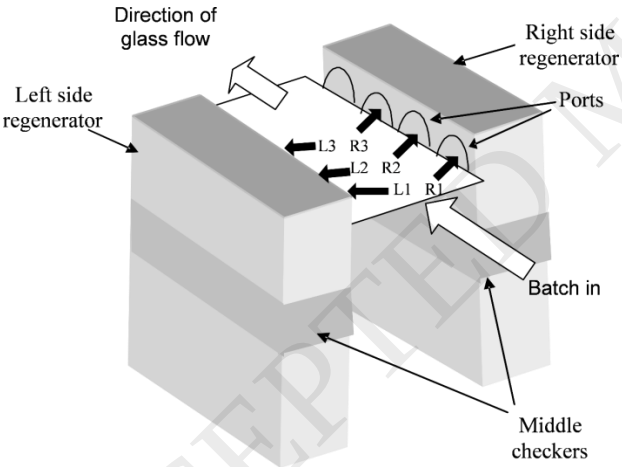

Figure 2. Sketch showing the position of the ports and middle checkers in the furnace

2. Method

Unused and used AZS samples from two float-glass furnaces (F1 and F2) were examined visually using optical microscopy and compared to virgin material to ascertain the degree of physical degradation. Backscattered scanning electron microscopy (SEM) was used to compare the microstructure of the unused and ex-service materials using a JEOL JSM 840A electron microscope.

IR spectroscopy, EDA, XRF and x-ray diffraction (XRD) were used to identify corrosion products. A Nicolet Impact 400 Spectrometer was used to carry out IR spectroscopy. The signal was plotted via OMNIC software. XRD was done with a Philips PW1730/10 x-ray diffractometer. Scans were carried out between 2θ values of 5° and 90° using a copper K_α source of wavelength 1.5418 Å with a step size of 0.02° and a

dwell time of 2 seconds per step. Phase identification was carried out by comparing the patterns with those held on a database produced by the International Center for Diffraction Data (I.C.C.D.). The software used to process and display the diffraction patterns was DRXWin 2.2.51. XRF analysis was carried out using the fused bead method and was expressed as percentage oxide. Energy dispersive analysis (EDA) was used, through an attachment to the electron microscope, to produce a ternary phase diagram using INCA Energy software. Chemically distinct areas were identified and were mapped onto the corresponding area on a scanning electron micrograph.

The permeability of samples was measured using the British Standard method, BS1902 section 3.9 (1995) [16]. The British Standard method for measuring bulk density and apparent porosity of dense refractory materials BS-EN 993-1 (1995) [17] was used.

The validity of analysis of the materials with variations in composition was ensured by confirming the results of the micro-analysis techniques (SEM and EDA) with the bulk spectroscopy techniques. Whole samples were powdered for this purpose to give homogeneity.

3. Results

The permeability to air of a cylindrical piece of virgin AZS was measured through the surface of the piece that would be exposed, in service, to the regenerator atmosphere. It was found to have a very low mean permeability of 7.75×10^{-13} cm^2. In an intact block the entire outer surface is covered in a continuous glass "skin" that seals the block making it impermeable. This continuous layer acts as a protective barrier to corrosive liquids or gases during service. The bulk density was measured as 3.3 ± 0.28 kg dm^{-3}.

The chemical composition by determined by XRF spectroscopy (Table 1) of virgin material was found to be approximately 15 % silica, 30 % zirconia and 53 % alumina. During analysis, the amount of SO_3 loss on ignition and fusion was found to be as high as 11.81 %. This is coupled with 15.10 % sodium oxide. This occurs in the material that exhibited the greatest degree of corrosion (Right Port 3 of F1).

	Oxide %							
	Virgin	F1 Port 1		F1 Port 2		F1 Port 3		F2
		Right	Left	Right	Left	Right	Left	
SiO_2	14.93	13.01	14.24	14.34	13.86	11.00	13.23	10.88
TiO_2	0.07	0.05	0.06	0.06	0.06	0.04	0.05	0.05
Al_2O_3	52.68	45.86	50.36	49.09	47.34	38.62	46.23	39.12
Fe_2O_3	0.06	0.05	0.07	0.05	0.05	0.07	0.11	0.1
CaO	0.06	0.38	0.08	0.06	0.08	0.08	0.19	0.12
MgO	0.02	0.11	0.02	0.02	0.02	0.04	0.08	0.13
K_2O	0.02	0.04	0.05	0.05	0.06	0.03	0.05	0.34
Na_2O	0.66	11.87	4.42	5.91	7.61	15.10	7.91	15.66
P_2O_5	0.05	0.03	0.04	0.06	0.04	0.04	0.04	0.15
Cr_2O_3	0.01	0.01	0.01	0.01	0.01	0.01	0.01	0.17
ZrO_2	29.91	26.93	29.51	29.43	28.19	22.55	26.73	22.85
HfO_2	0.69	0.57	0.62	0.62	0.60	0.47	0.55	0.51
CuO	0.03	0.01	0.01	0.01	0.01	0.01	0.01	0.01
L.O.I.*	0.00	0.95	0.10	0.11	1.12	11.81	0.65	9.84

Table 1. XRF analysis AZS checker material from F1, F2 and C1, *LOI is loss on ignition at 1025°C

Examination using XRD showed that monoclinic zirconia (baddeleyite), tetragonal zirconia and alpha alumina (corundum) are the main components of the virgin material (Table 2). XRD also confirmed chemical changes caused during service. The identification of corrosion products was confirmed using IR spectra (Figure 3 and Table 3).

I.C.C.D. No.	Formula	Name	Virgin AZS	L1	L2	L3	R1	R2	R3	F2
46-1212	Al_2O_3	Alumina (corundum)	*	*	*	*	*	*	*	*
36-420	ZrO_2	Zirconia (monoclinic)	*	*	*	*	*	*	*	*
42-1164	ZrO_2	Zirconia (tetragonal)	*	*	*	*	*	*	*	*
44-823	Na_2S_5	β sodium sulphide					*			
5-631	Na_2SO_4	Thenardite (syn)			*	*	*			*
17-538	$Na_8Al_6Si_6O_{24}SO_4$	Nosean		*		*				
46-103	$Na_7Al_6Si_6O_{24}S_3$	Sodalite (ultramarine)								*
110-221	$NaAlSiO_4$	Sodium aluminium silicate		*		*	*			
35-424	$NaAlSiO_4$	Nepheline		*			*	*	*	*
47-320	$NaAl_6O_{9.5}$	Sodium aluminium oxide			*	*	*			
21-1095	$NaAl_7O_{11}$	Sodium aluminium oxide								*
1-613	$Al_6Si_2O_{13}$	Aluminium silicate (mullite)	*							
37-1460	$Al_{0.5}Si_{0.7}O_{2.25}$	Aluminium Silicate 1			*	*				
29-84	$AlSi_{0.5}O_{2.5}$	Aluminium Silicate 2				*				
33-18	$Al(OH)_3$	Aluminium hydroxide							*	

Table 2. Summary of XRD analysis on virgin and used AZS

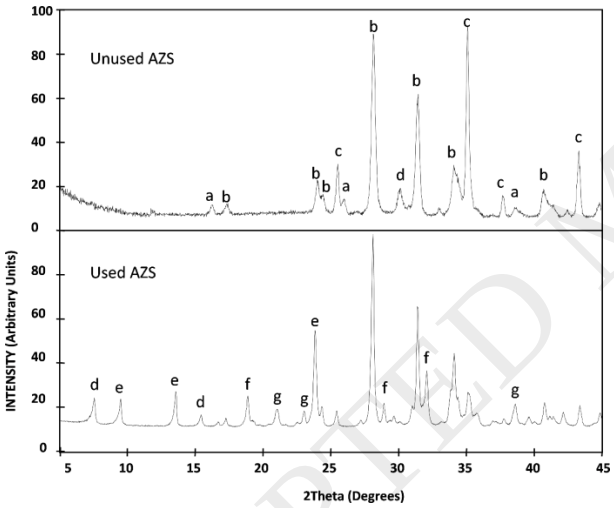

Figure 3. XRD of Unused and used material (F2) showing the peak positions of: a) mullite; b) monoclinic zirconia; c) alpha alumina; d) beta′ alumina; e) sodalite; f) sodium sulphate; and, g) nepheline

In the IR spectra for virgin AZS (Figure 4) a broad band at 1071 cm^{-1} corresponds to a combination of the symmetric Si-O-Si stretching and asymmetric Al-O-Si stretching at a slightly lower frequency of alumino-silicate. The predominant monoclinic form of the zirconia is confirmed by the band at 414_cm^{-1} and the corundum by those at 641 and 601 cm^{-1} (corresponding to Al-O-Al stretching) (Table 3). The final band at 454 cm^{-1} results from contributions from metal-oxygen bonds.

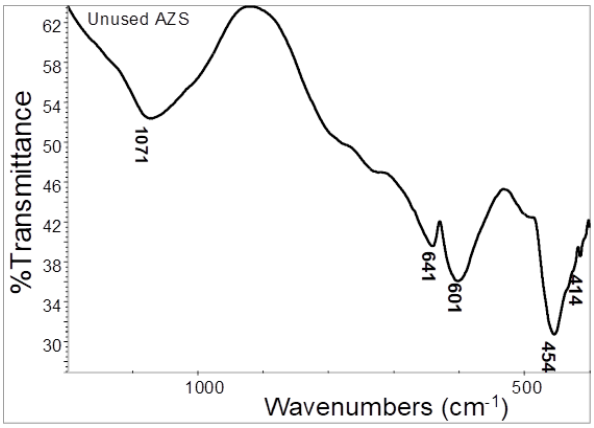

Figure 4. IR Analysis for virgin AZS

Bond	Virgin Material / cm^{-1}	Assignment and reference
Si-O	1071, 454	Alumino-silicate[18]
Al-O	641, 601, 454	Corundum [19]
	454	Alumino-silicate [18]
Zr-O	414	Monoclinic zirconia [20]

Table 3. Bond vibrations in virgin AZS

The IR spectra of used materials were consistent with XRD results confirming the formation of different aluminosilicates and the incorporation of sodium and sulphur (Table 4). In the spectrum of unused material a broad band at 454 cm^{-1} corresponds to Si-O and Al-O bending vibrations. This band split during service to give two sharper, separate absorption bands at 455 cm^{-1} and 423 cm^{-1}. These bands are due to the presence of remaining original corundum and sodalite. In nosean and haüyne, members of the sodalite series [22], these peaks are present as one diffuse peak [21, 23]. In ultramarine (also a member of the sodalite series) the absorption bands are present as two separate peaks [18]. The sharpening of the absorption bands in the spectra of sodalite can be attributed to increased ordering of the Al-Si bonding [18].

The absorption band at 1071 cm^{-1} in the virgin material has split and shifted to 1100 cm^{-1} and 1001 cm^{-1} in the F1 material. Absorption bands at 1100 cm^{-1} and 831 cm^{-1} are caused by the presence of sodium silicate glass ($Na_2Si_3O_7$) [25]. The signal at 1100 cm^{-1} is masked by the strong signal produced by absorbances produced by sodium sulphate at 1360 cm^{-1}. A similar situation is seen in F2.

The shift from 1071 cm^{-1} due to aluminosilicate in the virgin material to produce a broad absorbance at a lower frequency is consistent with the presence of nepheline [23, 24] and is due to a combination of asymmetric Al-O-Si stretching at 1001 cm^{-1}, symmetric Si-O-Si stretching at a slightly higher frequency and Al-O-Al symmetric stretching at a slightly lower frequency. This stretch moves to a lower wavelength as the relative amount of aluminium in the structure increases due to the decrease of silica. The band at 518 cm^{-1} is also characteristic of the presence of crystalline nepheline [24].

Bond	Virgin Material / cm^{-1}	Assignment	F1/ cm^{-1}	Assignment	F2/ cm^{-1}	Assignment
S-O			1199 1112 639 619	SO_4^{2-} Sodium sulphate [21]	1136 1100 639 617	SO_4^{2-} Sodium sulphate [21]
			1199 1112 729 698 658 619	Nosean [19]	1020	Sodalite [22, 18]
Si-O	1071 454	Alumino-silicate	994 454	Sodium aluminium silicate [18]	1001 455	Nepheline [23, 18, 24]
					455	Sodalite [22, 18]
					1100 831	Sodium silicate [25]
Al-O	454 601 641	Corundum	454	Corundum [19]	455	Corundum [24, 19]
	454	Alumino-silicate	994 698 454 430	Sodium aluminium silicate [18]	699 518	Nepheline [23, 18, 24, 26]
					980 757 699 669 455 423	Sodalite [22, 18]

Table 4. The IR spectra data of used AZS from F1 and F2

An absorption band consistent with the OH group stretching mode in $Al(OH)_3$, is present in R3 (Figure 5.), occurring between 3618_cm^{-1} and 3296 cm^{-1} resolved into six separate signals [26]. This is indicative of OH groups in gibbsite being situated within the layers of the crystal and forming hydrogen bonded bridges between the layers. The absorption bands at 3463 cm^{-1}, 3389 cm^{-1} and 3296 cm^{-1} in the IR spectrum of R3 correspond to OH bonds between adjacent layers and the bands at 3618 cm^{-1}, 3546 cm^{-1} and 3527 cm^{-1} correspond to the vibrations of longer hydrogen bonded OH groups within the layers.

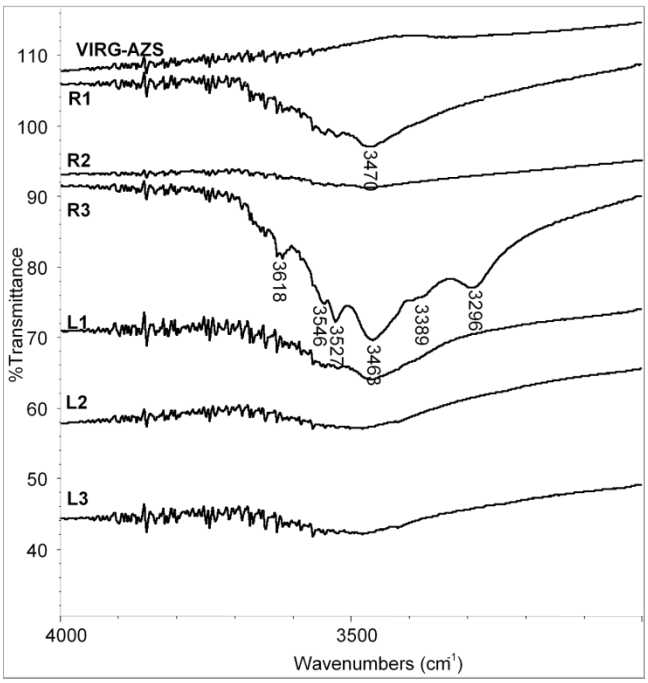

Figure 5. The IR spectra of used AZS from F1 showing the absorption bands of gibbsite in R3

In R3 (Figure 6.) bands at 1558 cm^{-1}, 1449 cm^{-1}, 1398 cm^{-1}, 881 cm^{-1} and the complex area between 735 and 615 cm^{-1} correspond to the presence of the carbonate, Na_2CO_3 [18].

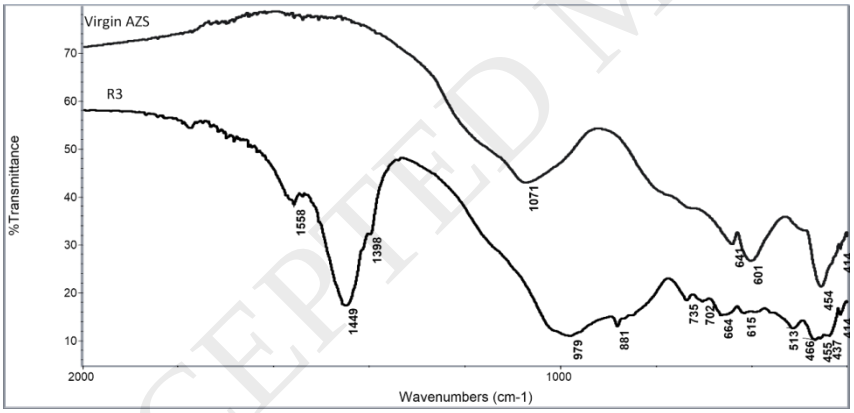

Figure 6. IR Spectra of unused AZS and R3 Microstructure

SEM was used to look at the microstructure of unused, F1 and F2 materials. EDA was used to look at elemental distribution. The elemental composition of an unused checker block was mapped at various depths below the surface of the block. The area near the surface that was mapped is shown in Figure 7.

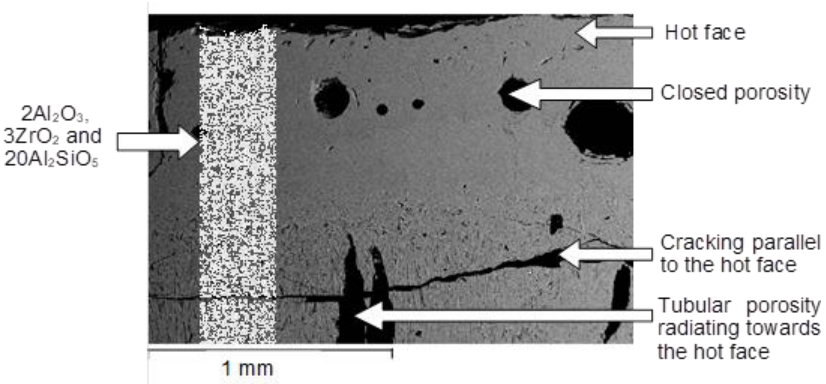

Figure 7. The near-surface of an unused AZS checker block with highlighted area showing the region mapped with EDA

The composition of the area mapped at the surface of an unused AZS checker block is shown in Table 5. in terms of percentage oxide. The typical measured error is approximately ±1 % of a given percentage oxide. The composition found is in very good agreement with that determined by XRF (Table 1). The relative ratios of the different oxides present in this mapped area correspond to a stoichiometric mixture of $2Al_2O_3$ (corundum), $3ZrO_2$ (zirconia) and $20Al_2SiO_5$ (mullite).

	Na_2O	**Al_2O_3**	**SiO_2**	**SO_3**	**ZrO_2**
MWT	*61.97*	*101.93*	*44.08*	*80.03*	*123.2*
Surface					
% Oxide	0.7	54.1	14.4	0	31.0
%ox/Mwt	0.0	0.5	0.3	0.0	0.3
Relative ratio	0	1.6	1.0	0.0	0.8
At 3mm					
% Oxide	1.4	53.4	16.7	0.0	29.1
%ox/Mwt	0.0	0.5	0.4	0.0	0.2
Relative ratio	0.0	1.4	1.0	0.0	0.6
At core phase 1					
% Oxide	0.9	67.0	3.1	0.0	30.6
%ox/Mwt	0.0	0.7	0.1	0.0	0.3
Relative ratio	0.0	2.6	0.3	0.0	1.0
At core phase 2					
% Oxide	1.4	47.0	21.2	0.0	30.7
%ox/Mwt	0.0	0.5	0.5	0.0	0.3
Relative ratio	0.0	1.9	1.9	0.0	1.0

Table 5. The composition of unused AZS near the surface shown with EDA analysis

At a depth of 3 mm from the hot face (Figure 8) Tubular pores originate and radiate towards the surface of the material from a definite boundary. Beyond this boundary, there is a dense, homogenous inner structure and no tubular pores.

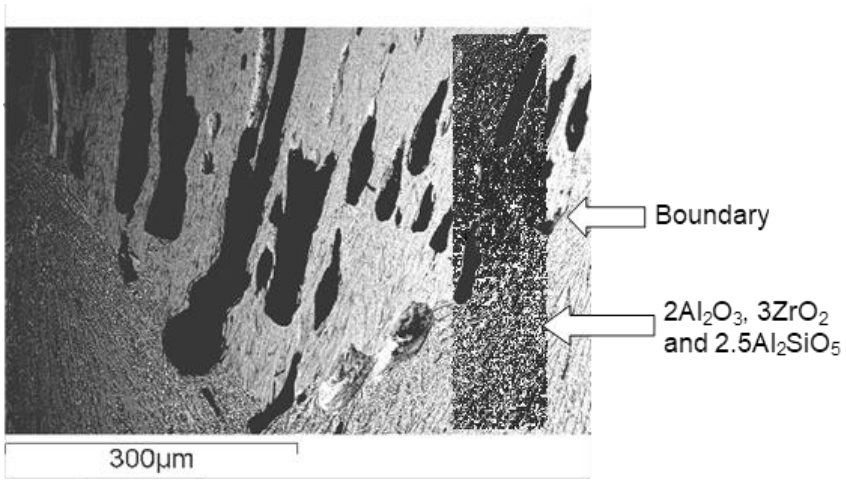

Figure 8. SEM image of unused AZS material 3 mm from the hot face with shaded area showing region analysed by EDA

Microscopy results were in agreement with the findings of the XRD analysis (Table 1) which showed the presence of zirconia (tetragonal and monoclinic), corundum and mullite (with a ratio of Al:Si of 3:1).

In the material from F1 SEM and EDA showed that both sulphur and sodium are present as sodium sulphate (Na_2SO_4) and nosean ($Na_8Al_6Si_6O_{24}SO_4$). Sodium is also present as sodium aluminium silicate ($NaAlSiO_4$) and sodium aluminium oxide ($NaAl_6O_{9.5}$). Analysis of a piece from the left Port 3 is shown in Table 6. Sodium noted as Na_2O in the analysis is likely to be bound to alumina and the aluminium silicate matrix.

Sodium aluminium oxide ($NaAl_6O_{9.5}$) is formed at the refractory surface with distinct areas. At 3 mm away from the hot face there is a region containing sodium, one containing both sodium and sulphur, and one resembling the original refractory containing no sulphur and a negligible amount of sodium. The distribution of the compounds in Table 6 is shown in Figure 9 and Figure 10.

	Na_2O	**Al_2O_3**	**SiO_2**	**SO_3**	**ZrO_2**	**Assignment**
MWT	*61.97*	*101.93*	*44.08*	*80.03*	*123.2*	
Hot face						
PHASE 1 % oxide	22.96	35.29	16.92	1.32	23.51	1.5 Al_2O_3 2 $NaAlSiO_4$ Na_2O ZrO_2
%ox/mwt	0.37	0.35	0.38	0.02	0.19	
ratio	1.94	1.81	2.01	0.09	1.00	
PHASE 2 % oxide	23	37.5	13.44	0.63	25.42	1.5 Al_2O_3 $NaAlSiO_4$ Na_2O ZrO_2
%ox/mwt	0.37	0.37	0.30	0.01	0.21	
ratio	1.22	1.21	1.00	0.03	0.68	
PHASE 3 % oxide	24.06	57.26	12.67	4.88	1.14	0.8 $Na_8Al_6Si_6O_{24}SO_4$ 0.2 Na_2SO_4 4 $NaAl_6O_{9.5}$
%ox/mwt	0.39	0.56	0.29	0.06	0.01	
ratio	6.37	9.21	4.71	1.00	0.15	
3 mm in						
PHASE 1 % oxide	19.12	36.76	14.56	0.65	28.91	$NaAlSiO_4$ 0.5 Al_2O_3
%ox/mwt	0.31	0.36	0.33	0.01	0.23	

ratio	1.00	1.17	1.07	0.03	0.76	0.5 Na_2O 0.75 ZrO_2
PHASE 2 % oxide	14.85	49.88	8.02	3.54	23.7	0.5 Na_2SO_4 0.5 $NaAl_6O_{9.5}$ 3.5 Al_2O_3 ZrO_2 $2NaAlSiO_4$
%ox/mwt	0.24	0.49	0.18	0.04	0.19	
ratio	1.32	2.69	1.00	0.24	1.06	
PHASE 3 % oxide	3.25	52.17	14.36	0.00	30.52	2.5 Al_2O_3 ZrO_2 Al_2SiO_5
%ox/mwt	0.05	0.51	0.33	0.00	0.25	
ratio	0.10	1.00	0.64	0.00	0.48	

Table 6. EDA analysis of used AZS material from F1

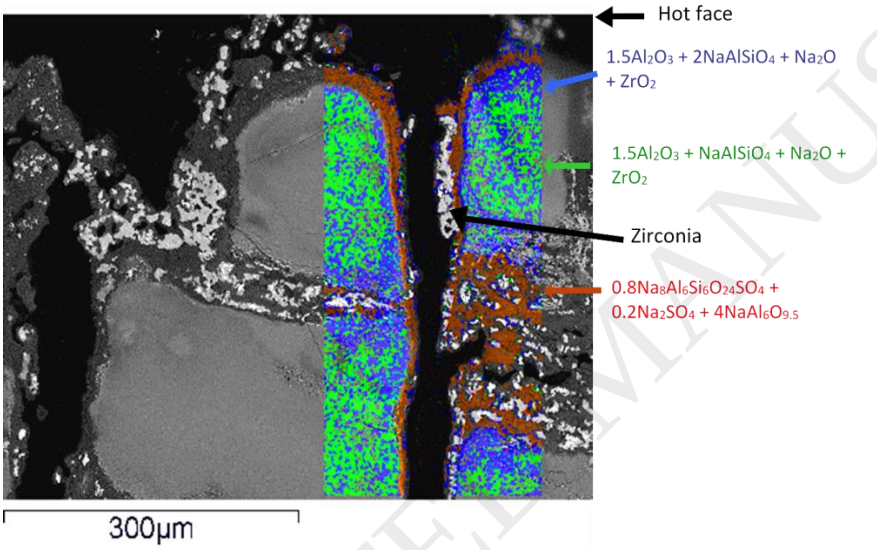

Figure 9. Colour-enhanced EDA map of the surface of used AZS, L3

The integrity of the surface is no longer intact as large channels are evident between the main parts of the material, giving the material a "finger-like" like appearance. The outer surfaces of the channels and cracks are coated in a film containing nosean and sodium sulphate and sodium aluminium oxide. This substance is devoid of aluminium silicate and dispersed zirconia. Zirconia has been deposited as large, recrystallised grains evident in the enlarged porosity.

At 3 mm into the material from the surface, sodium sulphate can be seen lining the pores (Figure 10). Whereas sulphur has remained at the surface of the material, either on the hot face of the block or lining the pores, sodium has penetrated into the bulk of the material where it has reacted with alumina and aluminium silicate to form sodium aluminium oxide at the interface and sodium aluminium silicate. A front can be seen to which sodium penetration has "soaked".

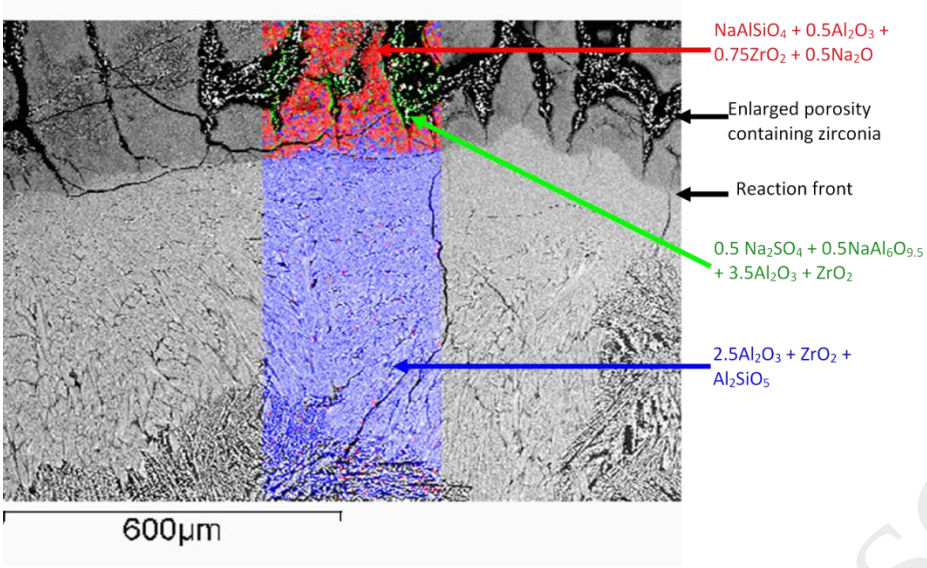

Figure 10. EDA map of used AZS (L3) 3 mm from the hot face

4. Discussion

The types of corrosion products formed on the left and right sides of the float glass furnace, F1, indicate that the conditions in the regenerators on the right side were more reducing than those on the left. A diagram showing the distribution of compounds across the furnace highlights this fact (Figure 11). It can be seen that where the conditions are more reducing, fewer corrosion products are formed and the severity of corrosion is less.

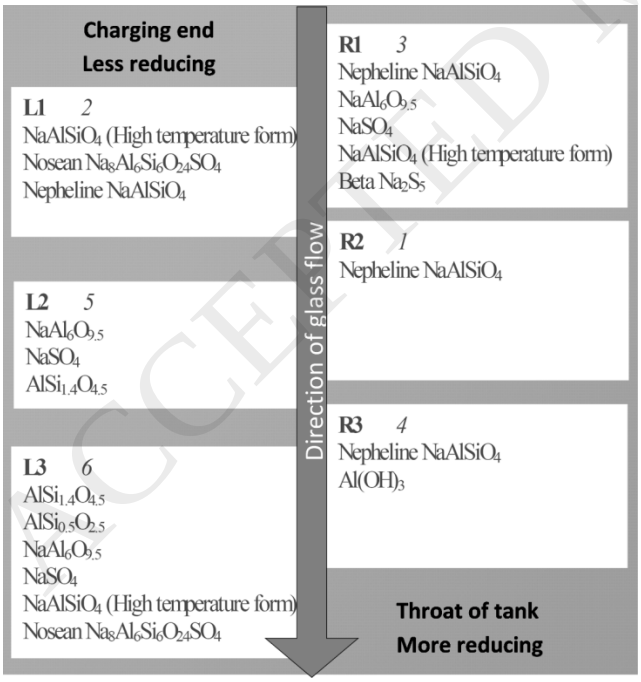

Figure 11. Diagram to show the distribution of corrosion products formed during service in F1 where the number in italics indicates the degree of resistance to corrosion (1>6)

Sodium sulphate (Na_2SO_4) was predominantly observed on the left hand side, whereas, the reduced sulphurous compound, β-sodium sulphide (Na_2S_5), deposited from the furnace atmosphere, was observed only on the right. Nosean ($Na_8Al_6Si_6O_{24}SO_4$) was only formed on the left side of the furnace according to the following reaction:

$$6NaAlSiO_{4(s)} + Na_2SO_{4(l)} \rightarrow Na_8Al_6Si_6O_{24}SO_{4\,(s)} \qquad \textbf{1.}$$

Sulphur was not incorporated into the original AZS regenerator material on the right hand side of the furnace at all. Crystalline aluminium silicates were only observed in material from the left side of this furnace. The materials containing these silica rich compounds exhibited a high degree of corrosion.

Sodium aluminium silicate ($NaAlSiO_4$) was formed on both the left and right sides of F1, although the cubic, high temperature form (usually formed above 1250 °C) was favoured on the left side and the hexagonal form (nepheline) was formed in all samples from the right. This implies that the temperature also tended to be higher on the left hand side of the furnace. Nepheline was the only corrosion product observed with XRD in the least corroded specimen, R2. It was not present in the two most corroded samples in which a high temperature form of $NaAlSiO_4$ was formed instead. In samples L1 and R1 both nepheline and the high temperature form were found.

Nepheline was also observed in material from F2. This furnace was also seen to have been subjected to a reducing atmosphere, shown by the detection of the sulphide, ultramarine, $Na_7Al_6Si_6O_{24}S_3$ (sodalite). The fact that sodium sulphate was detected in the sample from F2 also shows that the material had been at or below the temperature range of the "sulphate condensation zone" in the middle region of the region of the regenerator between 800 °C and 1000 °C. The fact that β′ alumina was detected in material from this furnace but not in that from F1 indicates that the conditions in F2 were hotter than those in F1.

No crystalline sulphur-containing compounds were found in the material from Ports 2 and 3 on the right hand side of the regenerator. Sodium-containing compounds, however, were present in both. This suggests that sodium sulphate was not responsible for corrosion in these samples. Na_2CO_3, which is prevalent in sodium-rich flue gas was identified via IR analysis. The formation of aluminium hydroxide in material from Port 3 (right side) suggests that a hydroxide such as sodium hydroxide rather than sodium sulphate was responsible for corrosion in this area of the furnace.

The sodium-containing region in the EDA map of L3, 3 mm featured increased microcracking. It is not clear whether the cracking was caused by the loss of the glassy phase and volume increase associated with the formation of sodium aluminium silicate, nosean and sodium aluminium oxide and subsequent temperature cycling, or whether the cracking occurred after service, as the piece cooled down.

Sodium aluminium oxide ($NaAl_6O_{9.5}$) converts to β´ and β´´ alumina above 950 °C. During the formation of sodium aluminium oxide ($NaAl_6O_{9.5}$) and β alumina from α alumina (corundum), there is a change in unit cell volume from that of corundum (Z=6) at 294 $Å^3$ to that of sodium aluminium oxide (Z=1) at 171 $Å^3$ and β´ alumina (Z=2) at 710 $Å^3$, where Z is the number of formula units within the unit cell. Per aluminium atom, this signifies a volume increase from 24.5 $Å^3$ to28.5 $Å^3$ and 50.7 $Å^3$ respectively.

It has also been observed that the formation of nosean from mullite is associated with an increase of 86% in the total volume of a refractory material [18]. The formation of nepheline and β alumina are both reported to be associated with a volume increase that is detrimental to the refractory block in which it occurs [27]. Cracking is therefore expected in this sample because the large volume changes that occur

during the formation of the corrosion products detected with XRD cannot be accommodated within the dense microstructure of AZS.

5. Conclusions

The material from the furnace, F1, had become severely degraded during service. It is shown that the independent attack of sodium or sodium sulphate was not responsible for the degradation of the checkers.

Sodium sulphate and other sodium-containing species, such as sodium hydroxide, were deposited onto the surface of the checkers and reacted with the blocks to form a complex mixture of compounds (confirmed by XRD) including hydroxides and compounds containing sulphur and sodium. The sulphur remained on and near the outside of the bulk of the material where the reactions given by equations **2**, **3** and **4** occurred with the sodium aluminium silicate components of the material to form nepheline, nosean and sodium aluminium oxide, which converts to β′ and β′′ alumina above 950 °C.

$$2Al_2SiO_{5(s)} + Na_2SO_{4(l)} \rightarrow 2NaAlSiO_{4(s)} + Al_2O_{3(s)} + SO_{3(g)} \quad \mathbf{2}$$

$$6NaAlSiO_{4(s)} + Na_2SO_{4(l)} \rightarrow Na_8Al_6Si_6O_{24}SO_{4\,(s)} \quad \mathbf{3}$$

$$3Al_2O_3\,(s) + 0.5Na_2O_{(g)} \rightarrow NaAl_6O_{9.5(s)} \quad \mathbf{4}$$

The formation of nosean from nepheline has been reported to be accompanied by an 86 % increase in volume. It is reasonable to assume that such a sizeable increase in volume of a component of the material at the surface of the block will have a detrimental effect and cause the material to quickly degrade revealing open tubular porosity beneath. This open porosity provides a direct route for corrosive agents to enter the material from the surrounding atmosphere and presents a large surface area for deposition and further reactions.

Sodium had diffused into the material and at a depth of several millimetres had reacted to form sodium aluminium silicates, nepheline and sodium aluminium oxide. Deeper into the bulk of the material sodium-containing compounds had reacted with corundum to form $NaAl_6O_{9.5}$, and mullite to form $NaAlSiO_4$.

Acknowledgements
This work was funded by the DTI and EPSRC and was carried out at Keele University. Financial support for this work and industrial support through the supply of corroded materials is gratefully acknowledged.

References

[1] V. Sardeshpande, R. Anthony, U.N. Gaitonde, R. Banerjee, Performance analysis for glass furnace regenerator, *Appl. Energy*. **88** (2011) 4451-4458.
[2] A. Abbassi, K. Khoshmanesh, Numerical simulation and experimental analysis of an industrial glass melting furnace, *Appl. Therm. Eng*. **28** (2008) 450-459.
[3] O. Auchet, P. Riedinger, O. Malasse, C. Iung, First-principles simplified modelling of glass furnaces combustion chambers, *Control Eng. Pract*. **16** (2008) 1443-1456.
[4] A. Li, Study on Structural Optimization Design of Heat Exchangers of Hot air furnace, *Energy Procedia*. **14** (2012) 1317-1322.
[5] Z. Li, X. He, Y. Wang, B. Zhang, H. He, Design of a flat glass furnace waste heat power generation system, *Appl. Therm. Eng*. **63** (2014) 290-296.
[6] V. Sardeshpande, U.N. Gaitonde, R. Banerjee, Model based energy benchmarking for glass furnace, *Energy Conversion and Management*. **48** (2007) 2718-2738.

[7] T.S. Busby,The Corrosion of Superstructure Refractories by Batch Materials. *Journal of the Society of Glass Technology* **40** (1956) 499T-508T.
[8] T.S. Busby, Porosity and Refractory Corrosion, *Journal of the Society of Glass Technology* **21**, (1957) 318T-329T.
[9] L. Petroni, M. Boussuge, D. Ryckelynck, Numerical simulation of the cooling-down of high-zirconia fused-cast refractories, *Journal of the European Ceramic Society*. **32** (2012) 3941-3947.
[10] P. Pena, E. Criado, J.J. Bakali, C. Baudín, Dynamic corrosion of Al2O3–ZrO2–SiO2 and Cr2O3-containing refractories by molten frits. Part II: Microstructural study, *Journal of the European Ceramic Society*. **31** (2011) 705-714.
[11] R.A. Rahimi, A. Ahmadi, S. Kakooei, S.K. Sadrnezhaad, Corrosion behavior of ZrO2–SiO2–Al2O3 refractories in lead silicate glass melts, *Journal of the European Ceramic Society*. **31** (2011) 715-721.
[12] C. Baudín, E. Criado, J.J. Bakali, P. Pena, Dynamic corrosion of Al2O3–ZrO2–SiO2 and Cr2O3-containing refractories by molten frits. Part I: Macroscopic analysis, *Journal of the European Ceramic Society*. **31** (2011) 697-703.
[13] C. Gault, F. Platon, D. Le Bras, Ultrasonic measurements of Young's modulus of Al2O3-based refractories at high temperatures, *Materials Science and Engineering*. **74** (1985) 105-111.
[14] E. Yeugo Fogaing, M. Huger, C. Gault, Elastic properties and microstructure: study of two fused cast refractory materials, *Journal of the European Ceramic Society*. **27** (2007) 1843-1848.
[15] C. Patapy, N. Gey, A. Hazotte, M. Humbert, D. Chateigner, R. Guinebretiere, M. Huger, T. Chotard, Mechanical behavior characterization of high zirconia fused-cast refractories at high temperature: Influence of the cooling stage on microstructural changes, *Journal of the European Ceramic Society*. **32** (2012) 3929-3939.
[16] BS-EN-993 (1995) Methods of Test for Dense Shaped Refractory Products, 993-1, “Determination of Bulk Density, Apparent and True Porosity”.
[17] British Standard 1902 (1981) Section 3.9: Refractory Materials "Determination of Permeability to Gases".
[18] Moenke, H. (1974). Silicates, the Three-Dimensional Silicates, Borosilicates and Beryllium Silicates. In *The Infrared Spectra of Minerals* (Farmer, V.C., ed.), The Mineralogical Society, pp. 365-374.
[19] Phillippi, C.M. (1970). Analytical Infrared Spectra of Particulate Alpha-aluminas. *Developments in Appl. Spectos.* **7B**, pp. 254-258
[20] Garrett, H.J. (1964). Infrared Absorption Spectroscopy in Zirconia Research. *Journal of the American Ceramic Society* **47**, pp. 622-624.
[21] Moenke, H. (1962). *Mineralspektren*, I. Academie-Verlag, Berlin.
[22] Deer, W.A., Howie, R.A. and Zussman, J. (1992). Sodalite Group. Sodalite, Nosean, Häuyne. In An Introduction to the Rock Forming Minerals, 2nd ed. pp. 496-502, Longman Scientific and Technical.
[23] Moenke, H. (1966). *Mineralspektren, II*. Academie-Verlag. Berlin.
[24] Sahama, T.G. (1965). Infrared Absorption of Nepheline. C. R. Soc. Geol. Finlande **37**, pp. 107.
[25] Hanna, R. (1964). Infrared Absorption Spectra of Sodium Silicate Glasses from 4 to 30 microns. *Journal of the American Ceramic Society* 47, pp. 597-601.
[26] Markovic, S., Dondur, V. and Dimitrijevic, R. (2003). FTIR Spectroscopy of Framework Aluminosilicate Structures: Canegieite and Pure Sodium Nepheline. *Journal of Molecular Structure* **654**, pp. 223-234.
[27] Weichert, T. (1986). Soda Lime Glass Furnace: Basic Refractory Checker Bricks in the Condensation Zone of Alkali Sulphates Lining and Service Requirements. *Interceram* **35**, pp. 10-13.

Figure captions.

Figure 1. Diagram to show the zones within the regenerator

Figure 2. Sketch showing the position of the ports and middle checkers in the furnace

Figure 3. XRD of Unused and used material (F2) showing the peak positions of: a) mullite; b) monoclinic zirconia; c) alpha alumina; d) beta' alumina; e) sodalite; f) sodium sulphate; and, g) nepheline

Figure 4. IR Analysis for virgin AZS

Figure 5. The IR spectra of used AZS from F1 showing the absorption bands of gibbsite in R3

Figure 6. IR Spectra of unused AZS and R3

Figure 7. The near-surface of an unused AZS checker block with highlighted area showing the region mapped with EDA

Figure 8. SEM image of unused AZS material 3 mm from the hot face with shaded area showing region analysed by EDA

Figure 9. Colour-enhanced EDA map of the surface of used AZS, L3

Figure 10. EDA map of used AZS (L3) 3 mm from the hot face

Figure 11. Diagram to show the distribution of corrosion products formed during service in F1 where the number in italics indicates the degree of resistance to corrosion (1>6)

Table 1. XRF analysis AZS checker material from F1, F2 and C1, *LOI is loss on ignition at 1025°C

Table 2. Summary of XRD analysis on virgin and used AZS

Table 3. Bond vibrations in virgin AZS

Table 4. The IR spectra data of used AZS from F1 and F2

Table 5. The composition of unused AZS near the surface shown with EDA analysis

Table 6. EDA analysis of used AZS material from F1